8-2016

Spectroscopic Investigation of Thermal Conductivity in Few-Layer Graphene

Joseph C. Denison Jr.
Clemson University, jcdenisonjr@msn.com

SPECTROSCOPIC INVESTIGATION OF THERMAL CONDUCTIVITY IN FEW-LAYER GRAPHENE

A Thesis
Presented to
the Graduate School of
Clemson University

In Partial Fulfillment
of the Requirements for the Degree
Master of Science
Physics and Astronomy

---

by
Joseph C. Denison Jr.
August 2016

Accepted by:
Dr. Ramakrishna Podila, Committee Chair
Dr. Apparao Rao
Dr. Sriparna Bhattacharya

ABSTRACT

Carbon is an extremely versatile element due to the ability of its electronic structure to allow strong bonds with many elements including other carbon atoms. This allows for the formation of many types of large and complex architectures, such as fullerenes and carbon nanotubes, at the nanoscale. One of the most fascinating allotropes of carbon is graphene, a two-dimensional honeycomb lattice with carbon in sp^2 hybridization, which building block for layered graphite and other nanocarbons.[1] Because of its unique structure, graphene displays several interesting properties including high thermal[2–4] and electrical mobility and conductivity[1,5]. The initial studies on graphene were performed on mechanically exfoliated samples, which were limited to few microns in size. In the recent years, large areas of single- and few-layer graphene (~few cm x cm) are being produced by chemical vapor deposition technique for practical applications. However, chemical vapor deposition grown graphene is highly polycrystalline with interfaces such as edges, grain boundaries, dislocations, and point defects. This inevitable presence of defects in graphene influences its electrical and thermal transport. While many studies have previously focused on the influence of defects on electrical mobility and conductivity, there is little information on the influence of defects on the thermal properties of graphene. This study specifically investigates the effect of both intrinsic and extrinsic defects on the in-plane thermal properties of graphene using micro-Raman spectroscopy.

The in-plane thermal conductivity of few-layered graphene (FLG) was measured using Raman spectroscopy, following the work of Balandin *et al*. [4]The thermal

conductivity was estimated from a shift of the characteristic *G*-band of graphene as a function of the excitation laser power. The graphene samples were synthesized on nickel substrates using chemical vapor deposition, and transferred to copper TEM grids and scanned using a micro-Raman spectrometer. The density of defects in the samples was controlled using reactive-ion etching with monovalent Ar ions. Thermal conductivities were then calculated and compared to previous works. Defect amounts were also calculated and catalogued. Defects and thermal conductivities from the two grids used were compared to assess the impact of defects, both in the structure of the graphene itself and surface contamination, on the in-plane thermal conductivity.

This work gives preliminary evidences that both intrinsic and extrinsic defects have a detrimental effect on the thermal conductivity of graphene. Intrinsic defects impede phonon mobility, which carries heat across the structure while extrinsic defects such as surface contamination open up more avenues for out-of-plane heat loss. The preliminary results presented in this work warrant the need for a detailed theoretical and experimental investigation of the influence of different defects (e.g., dopants) on the thermal conductivity of single- and few-layer graphene samples.

ACKNOWLEDGMENTS

I would like to profusely thank my committee members, Drs. Apparao Rao, Ramakrishna Podila, and Sriparna Bhattacharya for their steadfast help and guidance throughout this project. I would also like to thank Dr. Mehmet Karakaya and Jingyi Zhu for their help in teaching me how to use important equipment and drafting the thesis. Finally I would like my dear wife Jessica for all her love and aid in this endeavor.

TABLE OF CONTENTS

Page

Table of Contents (Continued)

Page

LIST OF TABLES

Table Page

LIST OF FIGURES

Figure (continued) Page

CHAPTER 1: INTRODUCTION

1.1 GRAPHENE:

Allotropes of the carbon atom occur throughout nature and can also be synthesized in the laboratory. These allotropes include materials known for years such as diamonds and graphite and the more recently discovered C_{60} (Buckministerfullerene) and carbon nanotubes. Graphene is a two dimensional, single or few layers of graphite with sp^2 bonded carbon atoms arranged in hexagonal honeycomb lattice structure, as shown in Fig. 1. [1] In graphene, each carbon atom is about a =1.42 Angstroms from its three in-plane neighbors. The carbon atom forms three σ bonds with these in-plane neighbors and a fourth π-bond, which is oriented in the out-of-plane direction. Each atom has one of these π-bonds, which are then hybridized together to form π-band and π^*-bands (sp^2 hybri-dization).

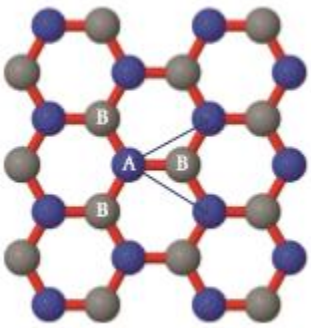

Figure 1. Single-layer graphene. Note the hexagonal structure as well as the Bernal AB stacking of the graphene lattice. [6]

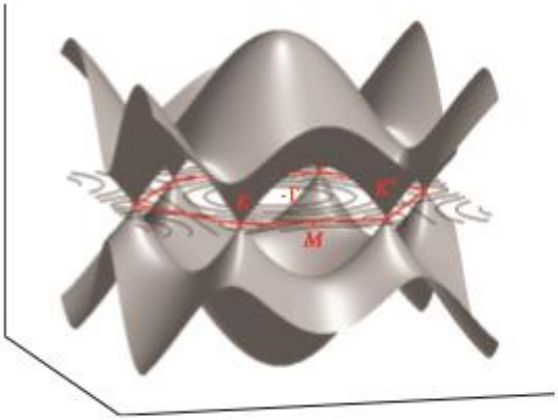

Figure 2. First Brillouin zone and band structure of graphene. [6]

In the honeycomb lattice of a single layer graphene sheet (SLG), there are two different triangular sub-lattice structures. Thus, one can consider graphene to be made up of a unit cell with two carbon atoms-one from each sub-lattice. Fig. 2 shows the First Brillouin zone and band structure of graphene. The vertical axis is electronic energy (*E*) while the horizontal plane below represents the momentum space. Since graphene is a 2D material there are only two dimensions of momentum space. [6] As shown in Fig. 2 graphene is a zero-gap semiconductor (or a semi-metal) because the conduction and valence bands connect at the so-called Dirac points. The Dirac points are locations in momentum (or *k*) space, on the ends of the Brillouin zone. [6] More importantly, graphene exhibits a linear E vs. k relation near the Dirac point unlike other the parabolic relation in other semiconductors. Because of this unique electronic structure, graphene displays a number of interesting electrical[1,5], mechanical[7], and thermal properties[2–4] and has attracted much attention.

1.2 RAMAN SPECTROSCOPY:

Raman spectroscopy uses the Raman Effect to non-destructively probe many types of materials. When most photons are scattered by an object they retain their incident frequency (elastic scattering/ Rayleigh scattering). The Raman Effect or Raman scattering results from a small amount of inelastic scattering of photons by interacting with molecular vibrations, or phonons in the material. This results in the photon having a different frequency and energy after scattering. During the Raman scattering process, at first an electron is excited by an incident photon from the material's valence band to a virtual or a real state with higher energy level. Secondly, the electron is scattered by interacting with phonons. Finally the electron relaxes back to its original state, and emits a photon. Due to the inelastic scattering process with phonons involved in the second step, the emitted photon exhibits lower (/higher) energy if the phonons are emitted (/absorbed), results into two distinct types of Raman scattering, Stokes and Anti-Stokes. Fig. 3 visually illustrates the Stokes and Anti-Stokes effects.

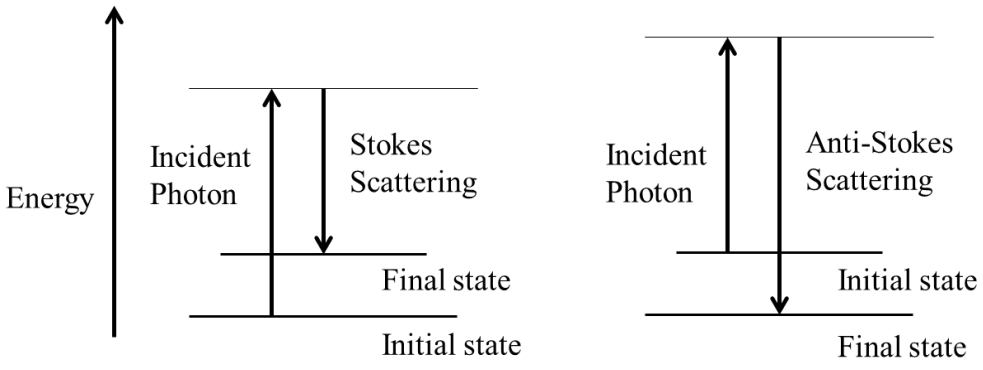

Figure 3. Visual representation of the difference between Stokes and Anti-Stokes scattering.

A resonance Raman scattering phenomenon occurs, when the photon absorption (or emission) forms a real electronic state. Resonance Raman signal is usually much higher (by a factor of 10^3) comparing to that of non-resonance Raman. It is well-known that nanocarbons such as single-walled carbon nanotubes and graphene exhibit resonant Raman features due to their unique electronic structure which provides real excited electronic states for many visible and near-infrared wavelengths.

1.3 RAMAN SPECTRA OF GRAPHENE:

Graphene has a characteristic Raman signature, which allows deep probing of its vibrational structure. As mentioned earlier, each unit cell of single layered graphene contains two atoms, which yields six different vibration modes, i.e. phonon branches (three acoustic and three optical). Fig. 4 displays the phonon dispersion relation of the 6 branches in SLG: out-of-plane tangential optical phonons (*oTO*), out-of-plane tangential acoustic phonons (*oTA*), in-plane tangential optical phonons (*iTO*), in-plane tangential acoustic phonons (*iTA*), longitudinal optical phonons (*LO*) and longitudinal acoustic phonons (*LA*).[8,9] Due to the small momentum of incident photons and rule of momentum conservation, photons usually only interacts with phonons has momentum $q \sim 0$ (near the Γ point, or zone center, in the phonon dispersion relation). In graphene, two optical phonon branches degenerate at the Γ point, *LO* and *iTO* are Raman active, which

result in one of the main feature in its Raman spectroscopy (see Fig. 5), i.e. the *G*-band around 1584 cm^{-1}.

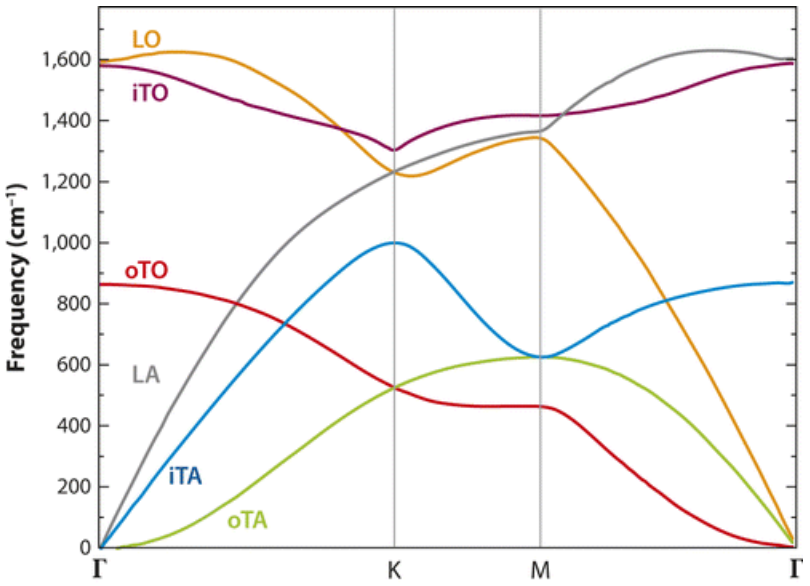

Figure 4. The phonon dispersion relation of the phonon branches in SLG. (Adapted from Ref [8])

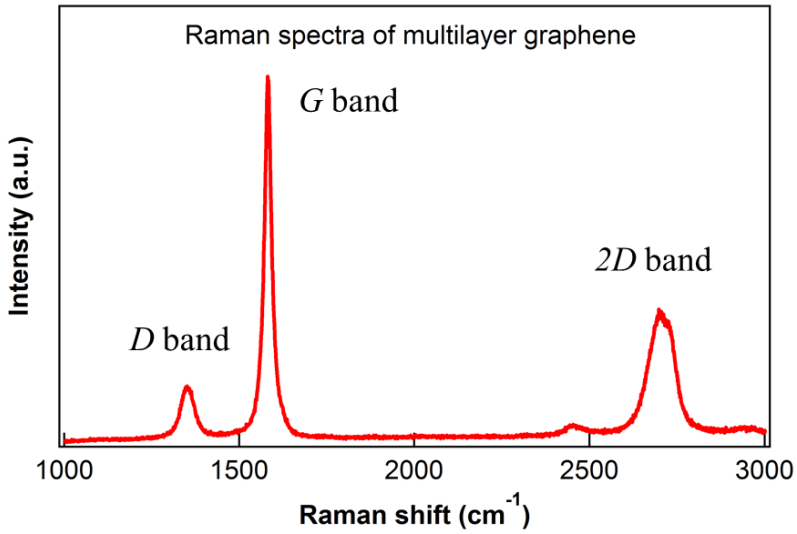

Figure 5. Raman spectra of multi-layer graphene with the three most apparent Raman peaks notated.

Fig.6 shows the schematic of electron-phonon resonance processes. The *G*-band is the only first order doubly degenerate (*iTO* and *LO*) phonon mode at the center of Brillouin zone. It has been shown that the *G*-band frequency is sensitive to temperature, charge transfer, as well as incident laser energy. However, clearly from Fig. 5 there are more features in the Raman spectra, such as the *D*- or disorder band ~ 1350 cm^{-1} and *G*'-band (or 2*D*-band or an overtone of *D*-band) ~ 2700 cm^{-1}. The peaks arise from a special electron-phonon resonance conditions – double-resonance process with phonon modes $q \neq 0$ due to the electronic structure of graphene. As shown in Fig. 6b, the *D*-band originates from a 2nd order process (Double Resonance or inter-valley process) with one phonon (*iTO*) and one defect near the *K*- or the Dirac point. In the process, the excited electron experienced one elastic scattering caused by a defect with no energy loss but a non-zero momentum change Δq and another inelastic scattering by a phonon with momentum $-\Delta q$. Comparing to the phonon dispersion relation (Fig. 4), the frequency of *D*-band corresponding to the frequency of an *iTO* phonon at *K* point. The intensity ratio of *D*-band to *G*-band (I_D/I_G) is generally used to quantifying the defects in graphene structure. The mean in-plane crystal size of graphene could be calculated by the following equation: [9,10]

$$L_a \text{ (nm)} = (2.4 \times 10^{-10} \text{ nm}^{-3}) \lambda^4_{laser} \text{ (nm}^4\text{)} \, (I_D/I_G)^{-1} \qquad (1)$$

The *G*'-band also originates from double resonance process as seen in Fig. 6c involving two *iTO* phonons near the *K* point. Therefore the frequency of the *G*'-band is almost double of that of the *D*-band, and so it is also denoted as 2*D*-band. By comparing

the intensity ratio of $I_{G'}/I_G$ and analyzing the peak components of *G*'-band, one can determine number of graphene layers. [9]

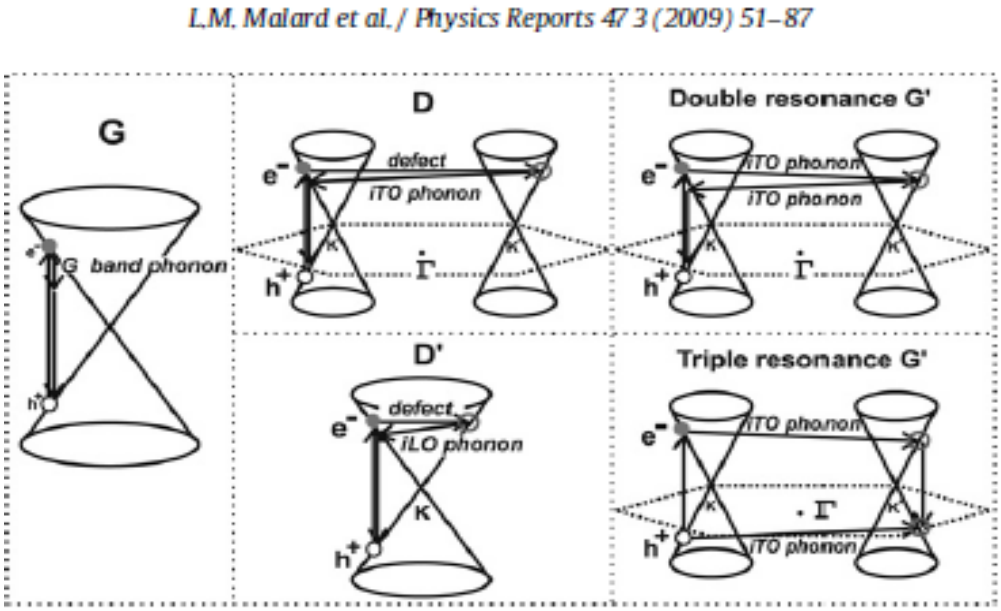

Figure 6. Generating processes for Raman peaks in graphene from L.M. Malard *et al.*[9]

1.4 UNIQUE THERMAL PROPERTIES OF GRAPHENE:

Graphene exhibits impressive thermal properties, where heat is carried by phonons, which have a high mobility due to strong in-plane sp^2 bonds. Graphene displays very high in-plane sound velocity, close to $c_{phonon} \approx 20$ km/s. [6] Using the kinetic theory of gases, the thermal conductivity due to phonons is given by $\kappa \sim c_{ph} C_V (T) \lambda$, where $C_V (T)$ is the specific heat per unit volume and λ is the phonon mean free path. [6] Hence, a large thermal conductivity is anticipated for graphene. This makes graphene a prime

candidate for a thermal interface material (TIM), which is used to enhance thermal coupling between two components. In addition to high thermal conductivity, graphene also exhibits unique mechanical and electrical properties. In case of graphite, thermal properties are anisotropic along the in-plane (high thermal conductivity) and out-of-plane (low thermal conductivity) direction. Here, we used few-layer graphene for exploring the influence of defects with an approximation that the thermal conductivity remains isotropic due to its quasi-2D nature.

1.5 DEFECTS:

Like any other material intrinsic and extrinsic defects can exist in graphene. Defects in the graphene structure are inevitable in grown graphene, particularly at the grain boundaries. (see Figure 7). In this investigation intrinsic defects are defects that occur within the graphene structure (e.g. discontinuities at grain boundaries) while extrinsic defects (e.g. dopants) and external defects (e.g. surface contamination) arise from heteroatomic elements and impurities (e.g. remnant polymer material used while etching graphene). Some of the unique properties of graphene can only be observed at an extremely low defect concentration (which is possible because of the high formation energies of point defects in graphene). It has been reported that by adding or tuning structures such as defects in graphene lattice could interestingly alter the properties of graphene, and even improve the performance in the application, such as magnetism[11–14], energy storage properties[15–17], electrical conductivity[6], and optical

properties[18,19]. For example, electrical properties of a perfect graphene sheet can be altered by defects, first by the introduction of spatial inhomogeneities in the carrier density and, second, by defects acting as scattering sources which reduce the electron mean free path.[6] Therefore, it could be both fundamentally and practically important to study the role of defects in graphene on its thermal conducting properties.

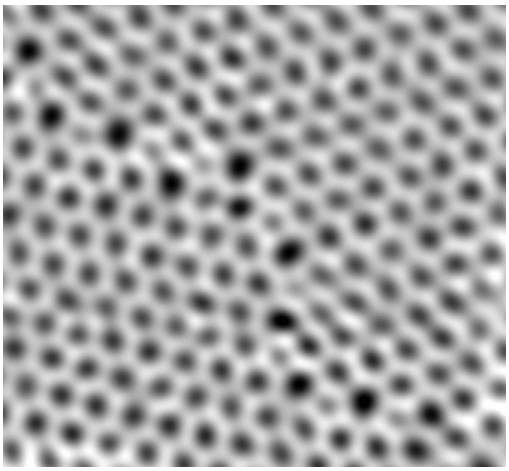

Figure 7. Grain boundaries of graphene from Huang *et al.* [20]

The central question of this thesis is how do intrinsic defects in the graphene structure, along with extrinsic defects such as surface contamination, specifically affect the in-plane thermal conductivity of few-layer graphene? Since defects in the structure of graphene decrease the phonon mobility, in effect the heat carrying capacity in-plane, it is expected that defects will have a deleterious effect on the thermal conductivity.

CHAPTER 2: BACKGROUND, EXPERIMENTAL METHODS, AND DATA ANALYSIS

2.1 BACKGROUND:

After its discovery, graphene was predicted to exhibit a high thermal conductivity (~ 2000 - 4000 $Wm^{-1}K^{-1}$) [2,21], which is greater than that of diamond. However, no feasible experimental methods existed at the time, to accurately determine the thermal conductivity of single layer graphene (SLG). In 2007, Calizo *et al.* [22] first investigated the temperature dependence of the frequency of the *G*-band peak position of graphene by using Raman spectroscopy that subsequently led to the experimental determination of the thermal conductivity of single layered graphene.

Calizo *et al*.[22] obtained single and bilayer graphene samples via micromechanical exfoliation of Kish graphite that were transferred to silicon substrates, coated with 300 nm SiO_2. In their experiments, a Renishaw micro-Raman spectrometer was used to measure the frequency of the *G*-band position while the temperature at the graphene samples was controlled using a liquid nitrogen cold-hot cell. Calizo *et al*. used low laser power (~4.8 mW) at top of cold-hot cell to avoid local sample heating. The temperature dependence of the *G*-band peak was measured for a temperature range of -190 °C to +100 °C (as shown in Figure 8).

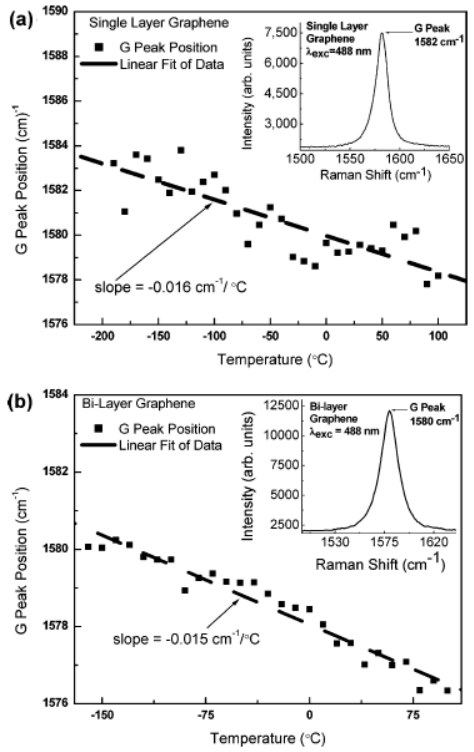

Figure 8: Temperature dependence of the *G* peak frequency for the single- (a) and bilayer (b) graphene. The insets show the shape of *G* peak. The measured data were used to extract the temperature coefficient for *G* peak (Calizo *et al.*[22])

As shown in Figure 8, increasing temperature led to the red shift of the *G*-band peak. The temperature dependence of the *G*-band frequency shift in graphene can be represented by the following simple relation:

$$\omega = \omega_0 + \chi T \qquad (2)$$

where ω_0 and ω represent the frequencies of the *G*-band peak positions extrapolated to 0 K and at a temperature *T* respectively, and χ is the first order temperature coefficient. The values of χ for several carbon based materials are shown in Table 1.

sample	χ (cm^{-1}/K)	λ_{laser} (nm)	heating method	temperature range (K)	reference
single-layer graphene	−0.0162	488	external	83−373	this work
bilayer graphene	−0.0154	488	external	113−373	this work
DWCNT	−0.022	647, 568, 515, 482	laser	180−320	Bassil et al.[20]
D-CNT	−0.023	632.8	laser	420−770	Huang et al.[17]
C-CNT	−0.028	632.8	laser	420−770	Huang et al.[17]
A-C	−0.027	632.8	laser	420−770	Huang et al.[17]
SWNT	−0.0189	514	external	299−773	Raravikar et al.[18]
CHOPG	−0.028	514.5	laser	286−647	Tan et al.[25]
HOPG	−0.011	514.5	laser	286−647	Tan et al.[25]
diamond	−0.012	406.7	external	300−1900	Zouboulis et al.[22]

[a] All data are for the *G* peak except for diamond, which is for the diamond peak at ~1332 cm^{-1}.

Table 1: Temperature coefficient for Carbon-Based Materials Table from Calizo *et. al.* [22]

It is important to note from Table I that the χ values of SLG and HOPG are of comparable magnitudes and their difference is quite small ~0.0152 cm^{-1}/K. For the measurements of multi-layer graphene in this thesis, an average of the two χ values is assumed, with appropriate error bars.

Subsequently, Balandin *et al.*[4] discovered a method of determining the thermal conductivity of graphene using its characteristic Raman signature and in particular its *G*-band temperature dependence and also the dependence of the *G*-peak frequency on the excitation laser power. As discovered by Calizo *et al.*, the *G*-band peak position shifted linearly with temperature.[22] The local temperature change produced by the variation of the laser excitation power focused on the graphene layer could then be used to calculate the thermal conductivity of graphene.

In Balandin's experiments, the exfoliated single layer graphene samples were suspended over 3 μm wide trenches designed by removing the 300 nm SiO_2 coating on Si substrate (as shown in Figure 9a) with graphitic heat sinks on either side.

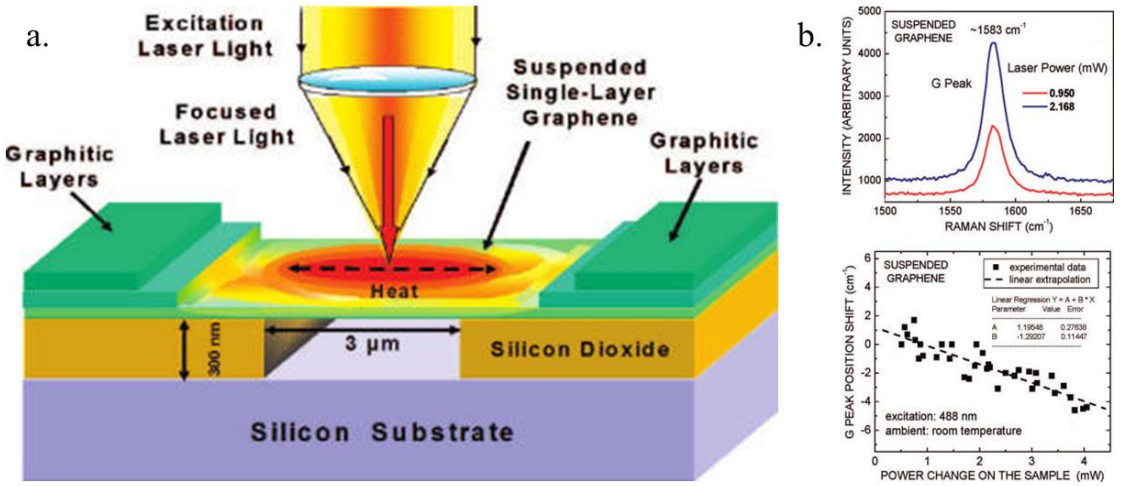

Figure 9. a. Schematic of the Balandin experiment showing the excitation laser light focused on a graphene layer suspended across a trench. The focused laser light creates a local hot spot and generates a heat wave inside SLG propagating toward heat sinks. b. Experimental data showing slope of change in *G*-band peak position vs. change in laser power. (Balandin *et al.* [4])

Below is a brief description of the Balandin's experimental setup. The laser beam was focused on the middle of the suspended graphene flake (~0.5-1.0 μm spot size) to heat the sample. Owing to the high thermal conductivity of graphene and negligible thermal conductivity of air (~0.025 W/mK), it could be assumed that the heat generated in SLG due to the laser excitation propagated laterally (or along the in-plane direction) through the SLG.[4] A small power dissipated in the center of the SLG can result in a temperature rise. Using the radial heat flow equation and the independently measured temperature dependence of the *G*-band peak position, and the dependence of the *G*-band frequency on the excitation laser power, the thermal conductivity of graphene was estimated using the following equation (see Balandin *et al.*[4] for further details):

$$\kappa = \chi_G \left(\frac{L}{2hW}\right)\left(\frac{\delta\omega}{\delta P}\right)^{-1} \quad (3)$$

In Eq. 3, κ stands for the thermal conductivity of graphene, χ_G is the temperature coefficient of *G*-peak of graphene, estimated for different graphene layers as shown in Table 1, [22] δω represents a small shift in *G*-band position as a result of the change δP in heating power on sample surface, *L* stands for the distance of the middle of the suspended SLG to the heat sink (graphitic layers) while *W* stands for the width of the graphene sample and *h* represents the thickness of the SLG. Figure 9b shows measurements of the slope (δω/δP) conducted by Balandin. Using this method thermal conductivity of SLG was calculated to be ~ $(4.84 \pm 0.44) \times 10^3$ to $(5.30 \pm 0.48) \times 10^3$ $Wm^{-1}K^{-1}$.

Following Balandin's work, the current study investigates the thermal conductivity of FLG suspended on TEM grids. Furthermore, the effect of defects on the thermal conductivity of graphene (via the incorporation of intrinsic defects by Reactive Ion Etching (RIE)), will be discussed in a later section.

2.2 EXPERIMENTAL METHODS:

In this work, graphene samples were synthesized using Chemical Vapor Deposition (CVD). The CVD of carbonaceous compounds onto transition metals has proven to be a most efficient method to synthesis graphene.[23] Not only has this method

produced high quality and large scale of graphene films but it also allows the grown graphene to be transferred to an arbitrary substrate.

The two main substrate metals used in the CVD process for synthesizing graphene are copper and nickel. Copper has low carbon solubility even at high temperatures and thus its surface likely acts as a catalyst for growth of single and bi-layered graphene. Nickel on the other hand has ~ppm carbon solubility and relatively high carbon diffusivity and therefore give rise of the growth of few-layer graphene (FLG).[24] Growth of FLG in nickel films will be highlighted in this thesis.

Two underlying processes occur in the CVD growth of FLG on nickel. First, carbon is thermally decomposed at high temperature from its gaseous precursor (CH_4) and dissolved into nickel at 800-900 ^{o}C. Second, carbon is crystallized in the form of FLG on the surface of the nickel, as the temperature is decreased to 400 ^{o}C initially and then to room temperature. The second process can occur both during the high temperature period or during cooling. A detailed description of the CVD process and the mechanism of growth may be found in Ref. [24].

This crystallization effect allows for purification of solid materials including carbon. The effect occurs when a solid (carbon) is placed in a solvent (nickel) that will not dissolve the solid unless the temperature is above the critical of phase transition. If that temperature is reached the carbon dissolves in nickel as the solvent and after a period of annealing as the temperature is reduced the pure carbon solid precipitates while the

impurities remain in the nickel solvent. This is what occurs during CVD growth of graphene on nickel.

The method of growing FLGs used in this thesis is as follows.[25] First nickel foil was placed inside of a 24 mm quartz tube. The position of the 25-micron thick nickel foil was just outside of the CVD tube furnace. As the furnace heats up to a temperature of 900°C gaseous Ar (230 sccm) and gaseous H_2 (120 sccm) is pumped into the furnace. Subsequently the Ni foil was moved to the center of the furnace. The furnace is maintained at 900°C for an hour in order to anneal the nickel. Then the temperature is dropped over a period of five minutes to 850°C. At 850°C gaseous CH_4 is introduced at 15 sccm for twenty-five minutes. Then the CH_4 is cut off and the furnace is allowed to slowly cool down to 400°C. Once this temperature is reached the H_2 is cut off. The furnace remains at this temperature for two hours and then is allowed to cool to room temperature. After this the nickel substrates were etched out by nitric acid and the FLG was transferred to the TEM grid.

2.3 TEM GRID:

A copper TEM (Transition Election Microscope) grid was used as the substrate for the investigation. Each grid has thousands of individual squares (grid points or "spots") of equal size. Graphene samples were suspended over these individual spots. Figure 10 shows a close up image of the grid taken through the microscope with an

individual “spot” highlighted. Individual spots are square with sides measuring 7.5 μm across.

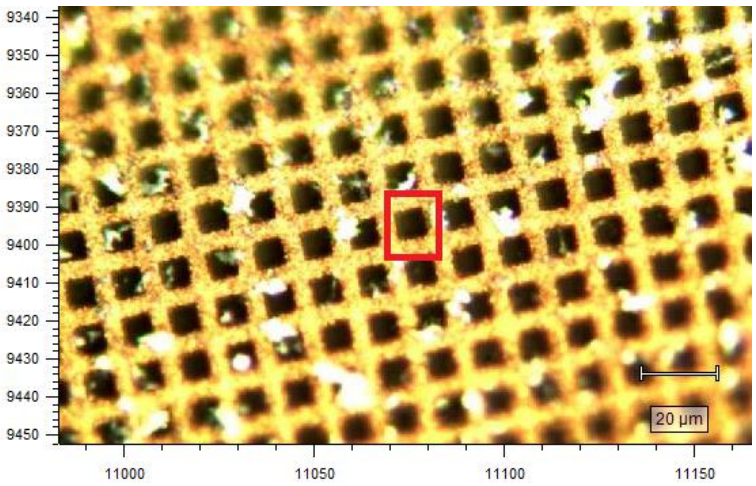

Figure 10. Graphene suspended over a TEM grid

Every individual side of the grid spot is a heatsink. This differs from Balandin’s investigation where only two of the four sides were heatsinks. This difference highlights one of the benefits of using a TEM grid to measure thermal conductivity of graphene. Balandin’s equation is dependent on the geometry of the substrate through the *L* and *W* variables. Since all sides of a TEM grid point are heatsinks and equal in length the *L* and *W* terms are reduced to a simple number (0.5) and the substrate geometry dependence of the equation is removed. Figure 11 shows examples of Raman spectra from selected spots on each TEM grid.

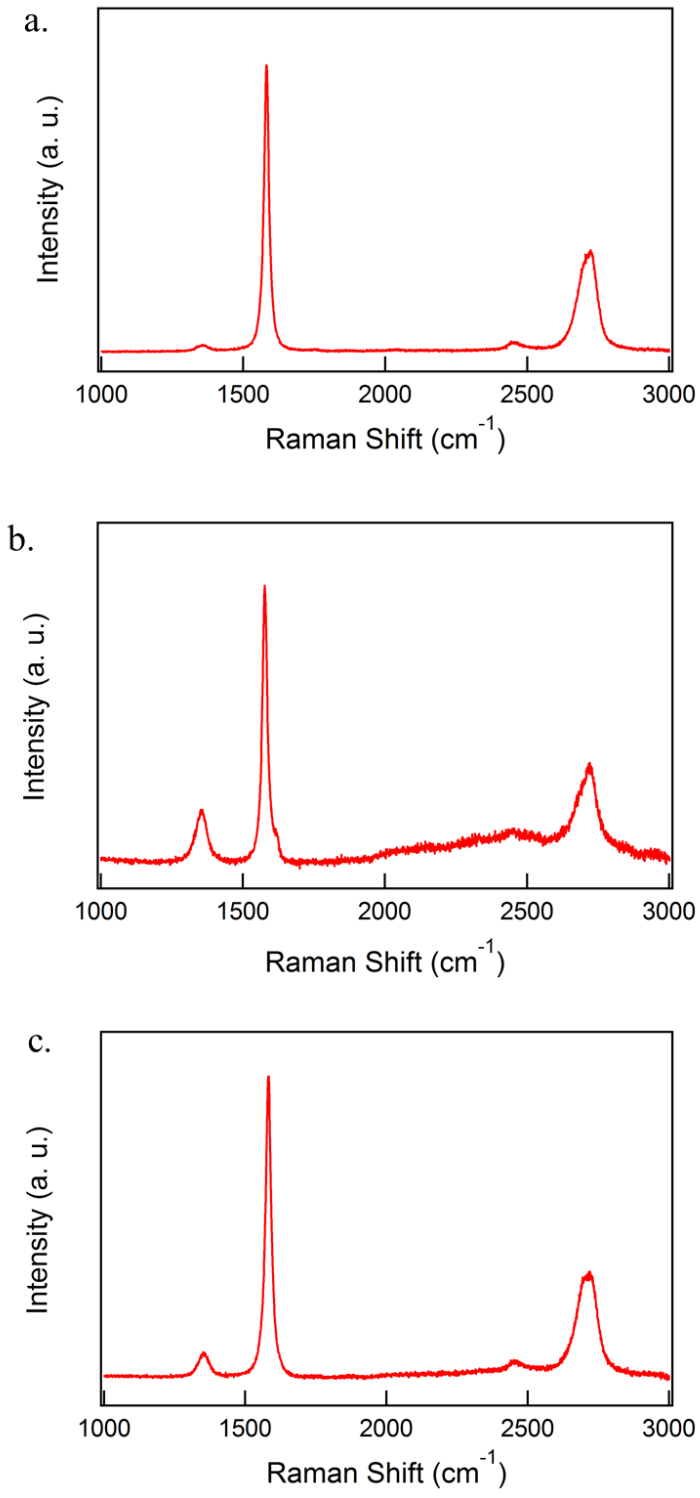

Figure 11. Sample Raman spectras from spots on each grid (a. Grid 2 (bf) spot 3 b. Grid 2 (af) spot 6 c. Grid 1 spot 5). All at 100% laser power.

2.4 MICRO-RAMAN SPECTROMETER

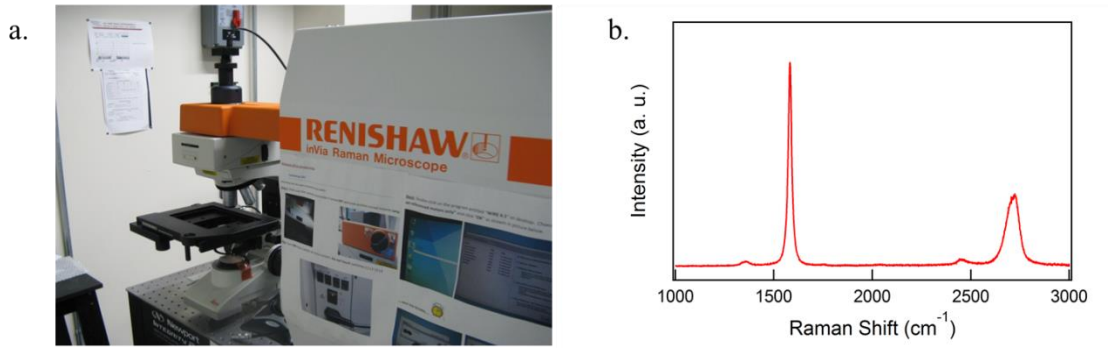

Figure 12. a. Image of a Renishaw micro-Raman spectrometer with in-Via microcope. b. Example Raman spectra from the spectrometer for a spot on the TEM grid

A Renishaw micro-Raman spectrometer was used to record the Raman spectra of FLG on TEM grid. For each investigation 3-6 spots on the grid were chosen for analysis. The presence of FLG at each spot used in this analysis was confirmed under optical microscope. As shown in Figure 12, the Raman signature of FLG is clearly seen by the presence of the *G*-band, *D*-band, and *G'*-band peaks.

Laser light from the spectrometer was then focused on the graphene flakes suspended over a spot using a Renishaw inVia Raman microscope with a 50X magnification. The spectrometer then performed a 25 second scan of the spot. For each spot several different laser power settings were used. Using filters in the spectrometer measurements were taken at 5%, 10%, 50%, and 100% laser power. Thus for each spot four scans were made at different laser powers.

It was determined that the laser light did not have the same power at the sample as it had at the source. Therefore the laser power was measured at both the source and the sample in order to determine the change in laser power at the sample.

Two TEM grids (labeled Grid 1 and Grid 2) were used in this experiment. Six spots were initially examined on Grid 2 and each spot was photographed after the examination. Grid 2 was then subjected to a Reactive Ion Etching (RIE) process (detailed below). This cleaned the grid of dirt and other contaminants while simultaneously creating defects in the graphene structure. After RIE (performed using Plasmaetch RE400) four more spots were examined and photographed on Grid 2. Five spots were investigated and photographed in the same manner on Grid 1. This grid was not subjected to RIE.

2.5 REACTIVE ION ETCHING:

Figure 13. Picture of Reactive Ion Etching (RIE) equipment

Reactive Ion Etching (RIE) is a dry etching process that uses Ar plasma to remove material from the surface of a sample. The sample is placed between two electrodes which accelerate ions toward the surface of the sample. Applied to graphene suspended over a TEM grid the RIE process cleans the surface of the grid and the graphene while adding defects into the graphene structure.

Grid 2 was first investigated and then subjected to 2 minutes of RIE at a power level of 80 Watts. This was done to study the difference increased defects in the graphene structure can have on its thermal conductivity. The increase in intrinsic graphene defects after RIE was confirmed using Raman spectroscopy and the I_D/I_G ratio.

2.6 DATA ANALYSIS:

The first step in data analysis was the determination of the *G*-band peak position for each data point. This was accomplished by the use of the software program Igor. After normalization of the individual spectra the *G*-band peak position was found using the Multipeak function for each measurement. Change in *G*-peak position was measured relative to the value of the *G*-band peak position at the 5% filter for that individual spot. Change in laser power was also measured relative to the 5% laser power measurement. All shifts in the *G*-band position relative to the 5% measurement were obtained and

plotted vs. the change in laser power. The slopes obtained from these graphs were used to calculate the thermal conductivity using Eq. 3. (Note: In the Balandin investigation the graphene was suspended between two heatsinks. On a copper TEM grid every side of each individual spot acts as a heatsink. Since the spots are square the length and width for each spot will be the same regardless of the orientation of the graphene. Thus L and W in the Balandin equation could be calculated from spot images and will always be related by a factor of 2)

Averages of all the G band shift data points for every spot were calculated for each value of the change in laser power. This resulted in a single data point for each value of change in laser power for each grid. These data points were then graphed with error bars ranging from the highest to the lowest values of the previous data points.

In Eq. 3 h represents the thickness of a single layer of graphene. Since this investigation deals with FLG (as analysis of the Raman spectra (intensity of G'-band vs. intensity of G-band) indicates) h in this context represents the thickness of the individual graphene layers plus the inter-layer spacing. A value of h = 2.4 nm was assumed as a midpoint value since each spot would have a different number of graphene layers.

Also using the Multipeak function on Igor the intensities of the G- and D-bands were measured for each data point. This allowed for I_D/I_G measurements to be taken for each spot. I_D/I_G ratios for individual spots were averaged for each grid. Thus the total I_D/I_G ratio for a grid is an average of all the I_D/I_G ratios for the individual spots on that

grid. These values were then compared to the thermal conductivity's calculated using Eq. 2.

2.7 STUDYING DEFFECT EFFECTS:

In order to study the impacts of both intrinsic and extrinsic defects on graphene thermal conductivity the two TEM grids used had different amounts of surface contamination. Grid 1 had a small amount of visible surface contamination (a "clean" grid) while Grid 2 had a larger amount as seen in Figure 14. Grid 2 was subjected to RIE, which induced intrinsic defects in the graphene structure and reduced surface contamination (as shown in Figure 14). This was done to study the difference in thermal conductivity of the same grid due to increased intrinsic defects. This will be shown in the results section.

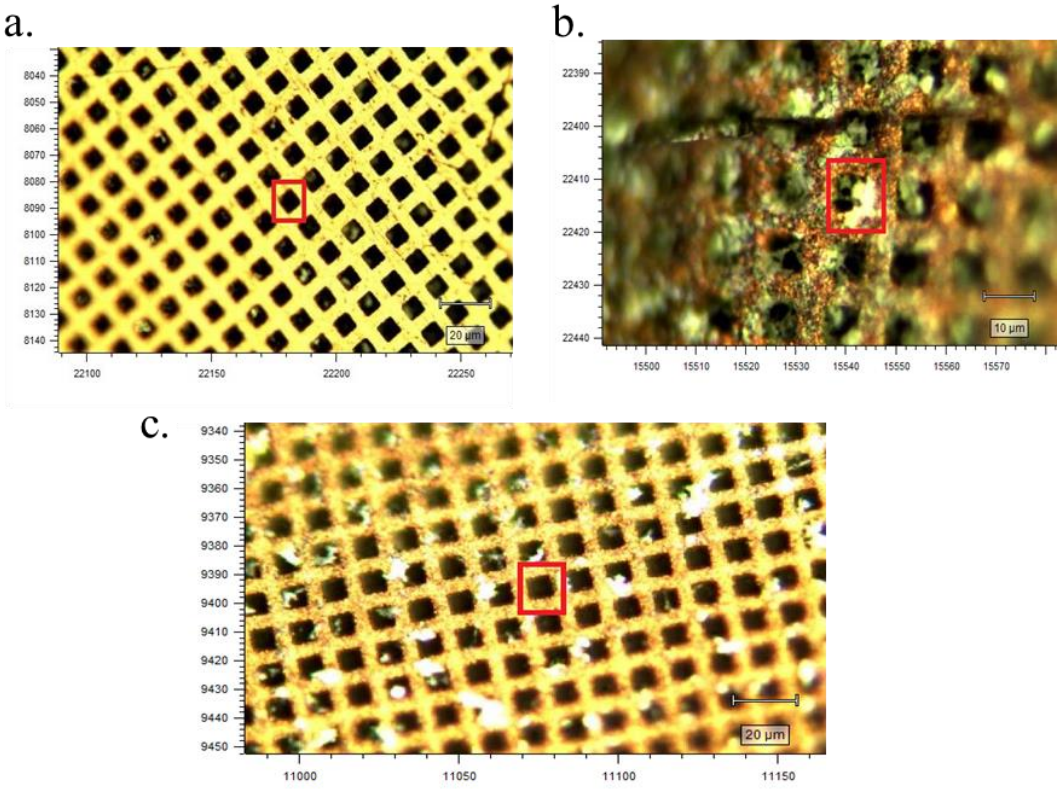

Figure 14 a. Close up on an example spot in Grid 1 showing the lack of surface contamination (clean grid). b. Close up on an example spot in Grid 2 before RIE showing the large amount of surface contamination. c. Close up on an example spot in Grid 2 before RIE showing the large amount of surface contamination.

CHAPTER 3: RESULTS, DISCUSSION, AND CONCLUSION

3.1 ANALYSIS OF IMPACT OF DEFECTS ON THERMAL CONDUCTIVITY:

The thermal conductivity values of graphene were estimated from Grids 1 and 2 before and after RIE (namely, Grid 2 (b) and (a) respectively), as discussed below. Figure 15 (a) exhibits the *G*-band shift as a function of change in laser power for Grid 1. As shown in Figure 15 (a), the measured slope ($\delta\omega/\delta P$) of the raw data points taking all spots on the TEM grid into account was ~ -0.71959 cm^{-1}/mW (inverse slope = -1.39 W/m·K). This negative slope is consistent with slopes found in Balandin's work (SLG inverse slope = -0.775 mW/cm^{-1}) [4]. To improve goodness of fit all data points for each change in laser power were averaged into a single data point. As shown in Figure 15 (b) the measured slope value remained unchanged while goodness of fit improved. No initial data points were removed. Using the above slope, κ_1 = 1906 ± 300 W/m·K was estimated using Eq. 1, assuming the layer thickness of graphene (*h*) equals 2.41 nm (~ 4 layers). For comparison the thermal conductivity for HOPG at RT is κ_{HOPG}= 1910 W/m·K [26] while the value for SLG from Balandin's work was $\kappa_{SLG} \approx$ 5000 W/m·K. [4]

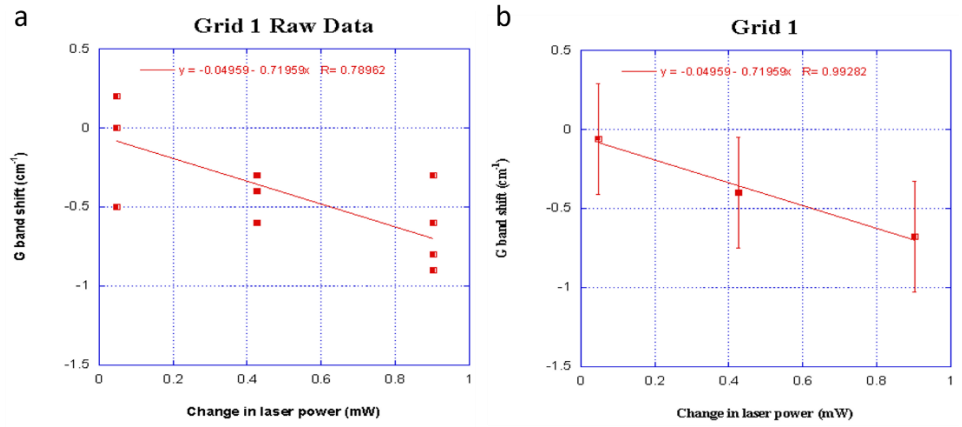

Figure 15 a. Graph of change in *G*-band position vs. change in laser power for all spots on Grid 1. b. Average change in *G*-band position vs. change in laser power for Grid 1.

Figure 16 (a) exhibits the *G*-band shift as a function of change in laser power for Grid 2 (b), before RIE, which displayed a negative slope ($\delta\omega/\delta P$) ~ -3.01 cm^{-1}/mW (inverse slope = -0.332 mW/cm^{-1}). The data showed some outliers, which were removed after careful analysis of the Raman spectra. Particularly, three data points (where the Raman spectral peaks showed more than 30% deviation) were removed from the initial data set due to a high amount of standard deviation as seen in Figure 16 (b). These points may be attributed to the drifting samples under the microscope due to the curvature of the grid. The change in laser power on this grid was lower than on Grid 1 due to a lower laser power incident on the sample. This was unavoidable due to the equipment at that time. All data points were averaged into a single data point for the same change in laser power as shown in Figure 17. Assuming the same graphene thickness, the thermal conductivity of graphene before RIE (Grid 2(b)), $\kappa_2 = 456 \pm 71$ W/m·K was ~76% lower than κ_1.

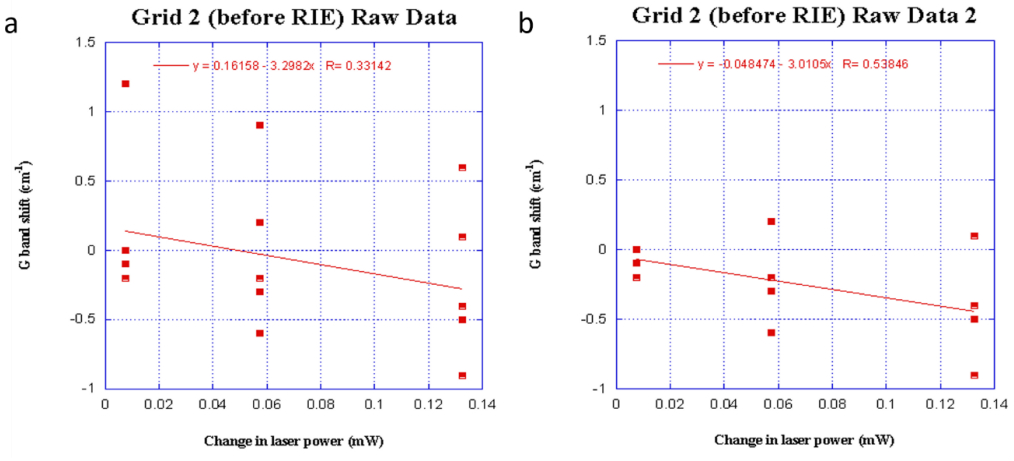

Figure 16 a. Graph of change in *G*-band position vs. change in laser power for all spots. b. Change in *G*-band position vs. change in laser power with all extraneous points removed.

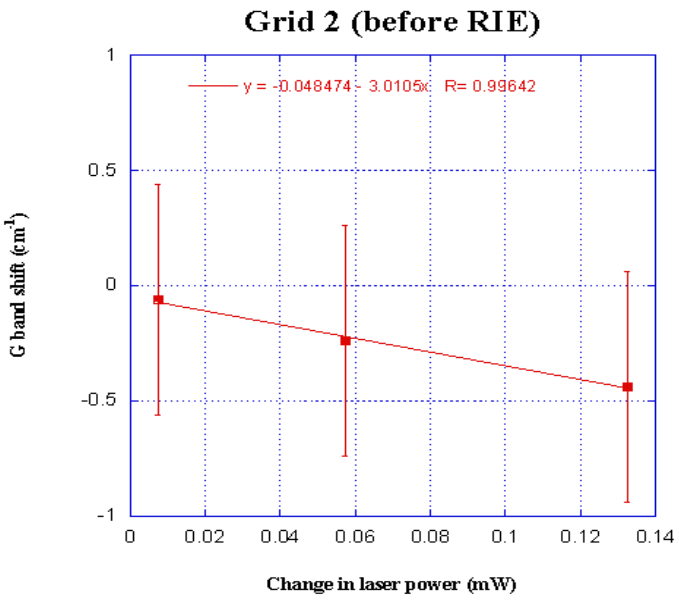

Figure 17. Average change in *G*-band position vs. change in laser power for Grid 2 before RIE.

Figure 18 (a) exhibits the *G*-band shift as a function of the change in laser power for Grid 2 after RIE, with a negative slope ($\delta\omega/\delta P$) ~ -4.23 cm^{-1}/mW and (inverse slope = -0.236 mW/cm^{-1}). The averaged *G*-band shift at each change in laser power is shown in Figure 18 (b). All data points from Fig. 18 (a) were included for averaging. The change in laser power for this sample was the same as that of Grid 1. The calculated thermal conductivity of graphene in Grid 2 (after RIE), κ_3 = 324 ± 50 W/m·K was ~ 29% lower (than Grid 2 before RIE and 89% lower than Grid 1, assuming the same thickness of graphene. The raw data points are listed in Tables 2, 3 and 4.

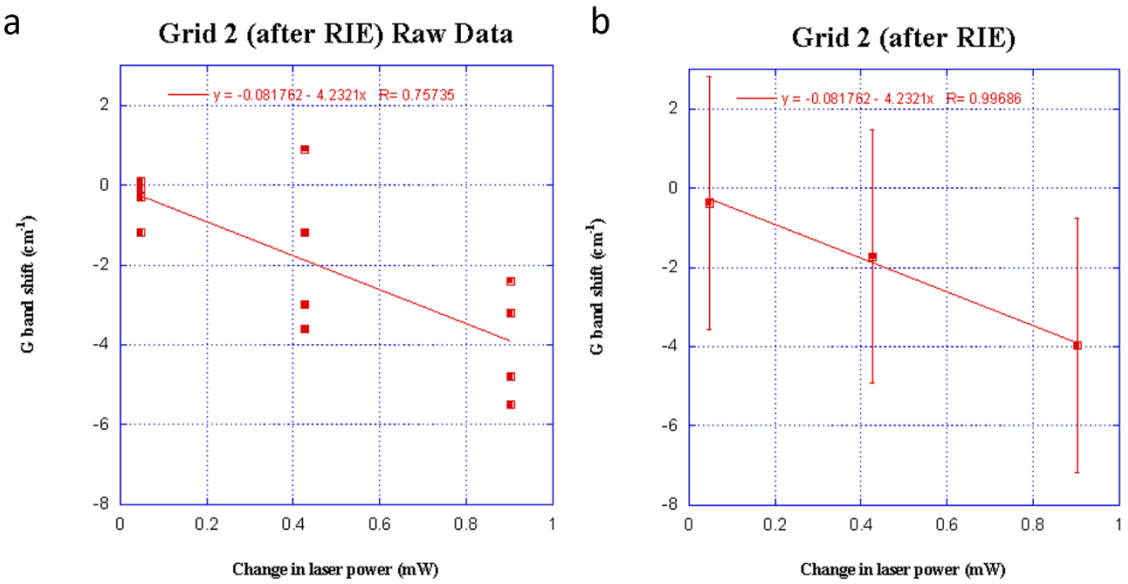

Figure 18 a. Graph of change in *G*-band position vs. change in laser power for all spots. b. Average change in *G*-band position vs. change in laser power.

Thermal conductivity of graphene on Grid 1 was the highest, κ_1~ 1906 W/m·K, compared to κ_2 on Grid 2 before RIE (where there were visible surface contaminations) and κ_3 where defects were induced on Grid 2 after RIE. This is possibly due to increased phonon scattering, with increase in defects. The κ of single layer graphene (SLG) measured by Balandin *et al*. [4] with the assumption that the heat was forced to propagate in the in-plane direction was comparatively higher. Nevertheless, our work shows that thermal conductivity values of few layer graphene (FLG), suspended on TEM grids were comparable to the previous work.

3.2 ANALYSIS OF IMPACT OF DEFECTS ON THERMAL CONDUCTIVITY

As noted in the Figure 19 (a) thermal conductivity of graphene on Grid 2 decreases 29% after RIE. Examination of the I_D/I_G ratio before and after RIE also shows a definite increase in the amount of intrinsic graphene defects in Grid 2 after RIE. This appears to show thermal conductivity decreasing in the presence of increased intrinsic graphene defects. However, Grid 1 displays a higher thermal conductivity than Grid 2 before and after RIE while also having a larger I_D/I_G ratio than Grid 2 before RIE, as shown in Figure 19 (b). This seems to call into question the conclusion that intrinsic defects inhibit thermal conductivity in graphene. Further investigation with carefully prepared single- and few-layer graphene samples and transferred without any polymer contamination is necessary to address the true influence of intrinsic defects.

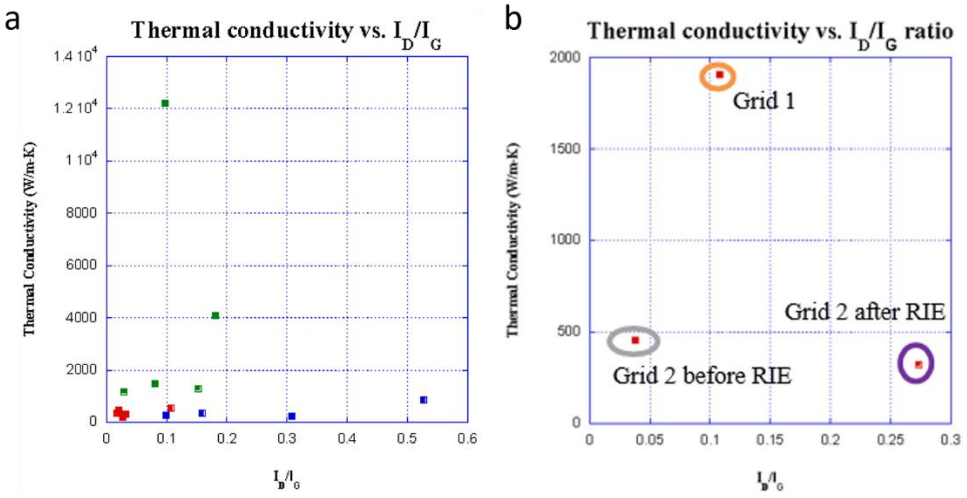

Figure 19. a. Red: Grid 2 before RIE, Green: Grid 1, Blue: Grid 2 after RIE. Thermal conductivity vs. I_D/I_G ratios for each individual spot. b. Calculated thermal conductivities for each grid vs. average I_D/I_G ratios for each grid.

The explanation for this apparent discrepancy lies in the amount of surface contamination on each grid. As noted above, Grid 1 was observed to have very low levels of visible surface contamination while Grid 2 before RIE displayed much higher levels of surface contamination. Large amounts of surface contaminants (resulting from the polymer remnants used for transferring the graphene layers) open numerous out-of-plane paths for heat to dissipate through. This kind of non-intrinsic defect lowers the in-plane thermal conductivity. In effect if Grids 1 and 2 were equally free of surface contamination Grid 2 should have a comparable thermal conductivity to Grid 1.

The data from these grids shows that intrinsic graphene defects (as well as non-intrinsic defects like surface contamination) have a detrimental effect on in-plane graphene thermal conductivity. A possible follow-on to this study would be to take a clean grid and a dirty grid and subject both to RIE. This would show more definitively the impact of non-intrinsic defects vs. intrinsic defects on the in-plane thermal conductivity.

3.3 SOURCES OF UNCERTAINTY

There were several sources of uncertainty in this investigation. The four sided heatsink of the TEM grid provided a larger avenue for heat losses than the two sided heatsink used by Balandin. Similarly in the Balandin investigation the heat flow could be assumed to be in-plane given that there was only one layer of graphene present. Here FLG was investigated so that assumption is inaccurate. Also in this work the exact

number of layers of graphene in each spot was not determined. Knowing the exact number of layers vs. taking an overall estimate for graphene thickness would greatly improve the accuracy of the thermal conductivity measurements.

Another source of uncertainty was that the laser focus point would drift very slightly during a scan with the micro-Raman spectrometer. Thus there is some uncertainty in amount of laser power incident on the sample. Also because of the limited number of filters on the spectrometer only three data points per spot could be obtained.

Even with these sources of uncertainty, the calculated thermal conductivities were comparable to previous results. This method also eliminates issues with previous measurements such as the geometry dependence of the Balandin equation. With refinements this method of measuring graphene thermal conductivity can be made even more accurate.

Table 2: GRID 1:

a. Spot # and % laser power	Shift in *G*-band peak (cm^{-1})	Change in laser power (mW)
Spot 2. 5% lp	0	0
Spot 2. 10% lp	0.2	0.0475
Spot 2. 50% lp	-0.3	0.4275
Spot 2. 100% lp	-0.8	0.9025

b. Spot # and % laser power	Shift in *G*-band peak (cm^{-1})	Change in laser power (mW)
Spot 3. 5% lp	0	0
Spot 3. 10% lp	0	0.0475
Spot 3. 50% lp	-0.4	0.4275
Spot 3. 100% lp	-0.8	0.9025

c. Spot # and % laser power	Shift in *G*-band peak (cm^{-1})	Change in laser power (mW)
Spot 4. 5% lp	0	0
Spot 4. 10% lp	0	0.0475
Spot 4. 50% lp	-0.3	0.4275
Spot 4. 100% lp	-0.3	0.9025

d. Spot # and % laser power	Shift in *G*-band peak (cm^{-1})	Change in laser power (mW)
Spot 5. 5% lp	0	0
Spot 5. 10% lp	0	0.0475
Spot 5. 50% lp	-0.4	0.4275
Spot 5. 100% lp	-0.9	0.9025

e. Spot # and % laser power	Shift in *G*-band peak (cm^{-1})	Change in laser power (mW)
Spot 6. 5% lp	0	0
Spot 6. 10% lp	-0.5	0.0475
Spot 6. 50% lp	-0.6	0.4275
Spot 6. 100% lp	-0.6	0.9025

f. Average Shift in *G*-peak for all spots (cm^{-1})	Change in laser power (mW)
-0.06	0.0475
-0.4	0.4275
-0.68	0.9025

Table 2: a-e. Raw data of G band shifts vs. change in laser power for all spots for Grid 1. f. Average of corrected G band shifts vs. change in laser power.

TABLE 3: GRID 2 BEFORE RIE:

a. Spot # and % laser power	Shift in *G*-band peak (cm^{-1})	Change in laser power (mW)
Spot 1. 5% lp	0	0
Spot 1. 10% lp	-0.2	0.0075
Spot 1. 50% lp	-0.2	0.0575
Spot 1. 100% lp	-0.5	0.1325

b. Spot # and % laser power	Shift in *G*-band peak (cm^{-1})	Change in laser power (mW)
Spot 2. 5% lp	0	0
Spot 2. 10% lp	0	0.0075
Spot 2. 50% lp	-0.3	0.0575
Spot 2. 100% lp	-0.5	0.1325

c. Spot # and % laser power	Shift in *G*-band peak (cm^{-1})	Change in laser power (mW)
Spot 3. 5% lp	0	0
Spot 3. 10% lp	0	0.0075
Spot 3. 50% lp	-0.6	0.0575
Spot 3. 100% lp	-0.9	0.1325

d. Spot # and % laser power	Shift in *G*-band peak (cm^{-1})	Change in laser power (mW)
Spot 4. 5% lp	0	0
Spot 4. 10% lp	1.2	0.0075
Spot 4. 50% lp	0.9	0.0575
Spot 4. 100% lp	0.6	0.1325

e. Spot # and % laser power	Shift in *G*-band peak (cm^{-1})	Change in laser power (mW)
Spot 5. 5% lp	0	0
Spot 5. 10% lp	-0.1	0.0075
Spot 5. 50% lp	0.2	0.0575
Spot 5. 100% lp	0.1	0.1325

f. Spot # and % laser power	Shift in *G*-band peak (cm^{-1})	Change in laser power (mW)
Spot 6. 5% lp	0	0
Spot 6. 10% lp	0	0.0075
Spot 6. 50% lp	-0.3	0.0575
Spot 6. 100% lp	-0.4	0.1325

g. Average Shift in *G*-peak for all spots (cm^{-1})	Change in laser power (mW)
-0.06	0.0075
-0.24	0.0575
-0.44	0.1325

Table 3: a-f. Raw data of G band shifts vs. change in laser power for all spots, g. average of corrected G band shifts vs. change in laser power

TABLE 4: GRID 2 AFTER RIE:

a. Spot # and % laser power	Shift in *G*-band peak (cm^{-1})	Change in laser power (mW)
Spot 1. 5% lp	0	0
Spot 1. 10% lp	-1.2	0.0475
Spot 1. 50% lp	0.9	0.4275
Spot 1. 100% lp	-2.4	0.9025

b. Spot # and % laser power	Shift in *G*-band peak (cm^{-1})	Change in laser power (mW)
Spot 4. 5% lp	0	0
Spot 4. 10% lp	-0.3	0.0475
Spot 4. 50% lp	-3.6	0.4275
Spot 4. 100% lp	-5.5	0.9025

c. Spot # and % laser power	Shift in *G*-band peak (cm^{-1})	Change in laser power (mW)
Spot 5. 5% lp	0	0
Spot 5. 10% lp	0.1	0.0475
Spot 5. 50% lp	-1.2	0.4275
Spot 5. 100% lp	-3.2	0.9025

d. Spot # and % laser power	Shift in *G*-band peak (cm^{-1})	Change in laser power (mW)
Spot 6. 5% lp	0	0
Spot 6. 10% lp	-0.1	0.0475
Spot 6. 50% lp	-3	0.4275
Spot 6. 100% lp	-4.8	0.9025

e. Average Shift in *G*-peak for all spots (cm^{-1})	Change in laser power (mW)
-0.375	0.0475
-1.725	0.4275
-3.975	0.9025

Table 4: a-d Raw data of *G*-band shifts vs. change in laser power for all spots, e. average of corrected *G*-band shifts vs. change in laser power

a. Grid 1. Spot #	I_D/I_G ratio	Thermal conductivity (W/m-K)
Spot 2.	0.0288	1175
Spot 3.	0.0813	1469
Spot 4.	0.1521	1301
Spot 5.	0.0976	4069
Spot 6.	0.1814	12204

b. Grid 2b. Spot #	I_D/I_G ratio	Thermal conductivity (W/m-K)
Spot 1.	0.1070	543
Spot 2.	0.0251	352
Spot 3.	0.0275	197
Spot 4.	0.0319	290
Spot 6.	0.0213	449

c. Grid 2a. Spot #	I_D/I_G ratio	Thermal conductivity (W/m-K)
Spot 1.	0.5260	841
Spot 4.	0.3085	229
Spot 5.	0.0991	253
Spot 6.	0.1589	354

d. Grid #	Average I_D/I_G ratio	Calculated Thermal conductivity (W/m-K)
Grid 1.	0.1082	1906
Grid 2b.	0.0377	456
Grid 2a.	0.2731411	324

Table 5 a-c: I_D/I_G ratios for each spot vs. thermal conductivities for each spot. d: Average I_D/I_G ratios for each grid vs. calculated thermal conductivities for each spot.

3.4 CONCLUSION

Graphene is a two-dimensional material carbon allotrope made up of a single layer of graphite that has many unique properties. The characteristic Raman spectra of graphene allowed intense studies to be undertaken. Among graphene's unique properties is a high phonon mobility, which allows heat to be carried easily along the in-plane direction. This results in a high-predicted in-plane thermal conductivity. After the discovery of graphene, ways to measure its extraordinary predicted properties were sought out. To determine the thermal conductivity of single layer graphene A.A. Balandin and I. Calizo developed a technique using Raman spectroscopy to measure the in-plane thermal conductivity of exfoliated single layer graphene suspended over a two-sided heat sink.

In this investigation graphene grown using chemical vapor deposition was placed on a copper TEM grid with each side of the grid spots being heatsinks. This eliminates the geometry dependence from previous work. The few layer graphene samples were investigated using Raman spectroscopy and the thermal conductivity calculated using the Balandin equation (Eq. 3). Thermal conductivities were found to be in-line with previous work.

The main goal of the investigation was to uncover the effects of intrinsic and extrinsic defects on the thermal conductivity of graphene. It was thought that increased defects in the graphene structure would inhibit the in-plane thermal conductivity. The I_D/I_G ratio from the Raman spectra of graphene was used to determine the amount of

intrinsic defects in each sample. Grids were selected with low and high surface contaminates to investigate effects of such contamination on the thermal conductivity. By performing Reactive Ion Etching on a sample (previously investigated) led to increased intrinsic defects and a method of reduction of thermal conductivity was uncovered. It has been shown that intrinsic defects do in fact impede the in-plane thermal conductivity. Also it was shown that surface contaminants provide an avenue for heat loss, which also adversely affects the thermal conductivity. Based on the encouraging preliminary results presented in this work, more detailed investigations are necessary to correlate the defect configuration and type with the changes in thermal conductivity.

REFERENCES

[1] A. K. Geim and K. S. Novoselov, "The rise of graphene.," *Nat. Mater.* **6**, 183–191 (2007).

[2] S. Ghosh, I. Calizo, D. Teweldebrhan, E. P. Pokatilov, D. L. Nika, A. A. Balandin, W. Bao, F. Miao, and C. N. Lau, "Extremely high thermal conductivity of graphene: Prospects for thermal management applications in nanoelectronic circuits," *Appl. Phys. Lett.* **92**, 2008–2010 (2008).

[3] K. Saito, J. Nakamura, and A. Natori, "Ballistic thermal conductance of a graphene sheet," *Phys. Rev. B* **76**, 115409 (American Physical Society, 2007).

[4] A. A. Balandin, S. Ghosh, W. Bao, I. Calizo, D. Teweldebrhan, F. Miao, and C. N. Lau, "Superior Thermal Conductivity of Single-Layer Graphene," *Nano Lett.* **8**, 902–907 (American Chemical Society, 2008).

[5] K. I. Bolotin, K. J. Sikes, Z. Jiang, M. Klima, G. Fudenberg, J. Hone, P. Kim, and H. L. Stormer, "Ultrahigh electron mobility in suspended graphene," 2008.

[6] D. R. Cooper, B. D'Anjou, N. Ghattamaneni, B. Harack, M. Hilke, A. Horth, N. Majlis, M. Massicotte, L. Vandsburger, et al., "Experimental Review of Graphene," *ISRN Condens. Matter Phys.* **2012**, 1–56 (2012).

[7] C. Lee, X. Wei, J. W. Kysar, and J. Hone, "Measurement of the elastic properties and intrinsic strength of monolayer graphene.," *Science* **321**, 385–388 (American Association for the Advancement of Science, 2008).

[8] M. Lazzeri, C. Attaccalite, L. Wirtz, and F. Mauri, "Impact of the electron-electron correlation on phonon dispersion: Failure of LDA and GGA DFT functionals in graphene and graphite," *Phys. Rev. B* **78**, 081406 (American Physical Society, 2008).

[9] L. M. Malard, M. A. Pimenta, G. Dresselhaus, and M. S. Dresselhaus, "Raman spectroscopy in graphene," *Phys. Rep.* **473**, 51–87 (2009).

[10] L. G. Cançado, K. Takai, T. Enoki, M. Endo, Y. A. Kim, H. Mizusaki, A. Jorio, L. N. Coelho, R. Magalhães-Paniago, et al., "General equation for the determination of the crystallite size L[sub a] of nanographite by Raman spectroscopy," *Appl. Phys. Lett.* **88**, 163106 (AIP Publishing, 2006).

[11] M. Sepioni, R. R. Nair, S. Rablen, J. Narayanan, F. Tuna, R. Winpenny, A. K. Geim, and I. V Grigorieva, "Limits on intrinsic magnetism in graphene.," *Phys. Rev. Lett.* **105**, 207205 (American Physical Society, 2010).

[12] R. R. Nair, M. Sepioni, I.-L. Tsai, O. Lehtinen, J. Keinonen, A. V. Krasheninnikov, T. Thomson, A. K. Geim, and I. V. Grigorieva, "Spin-half paramagnetism in graphene induced by point defects," *Nat. Phys.* **8**, 199–202 (Nature Publishing Group, 2012).

[13] Y. Wang, Y. Huang, Y. Song, X. Zhang, Y. Ma, J. Liang, and Y. Chen, "Room-temperature ferromagnetism of graphene.," *Nano Lett.* **9**, 220–224 (American Chemical Society, 2009).

[14] J. Zhu, H. Park, R. Podila, A. Wadehra, P. Ayala, L. Oliveira, J. He, A. A. Zakhidov, A. Howard, et al., "Magnetic properties of sulfur-doped graphene," *J. Magn. Magn. Mater.* **401**, 70–76 (2016).

[15] R. Narayanan, H. Yamada, M. Karakaya, R. Podila, A. M. Rao, and P. R. Bandaru, "Modulation of the Electrostatic and Quantum Capacitances of Few Layered Graphenes through Plasma Processing.," *Nano Lett.* **15**, 3067–3072 (2015).

[16] L. L. Zhang, X. Zhao, H. Ji, M. D. Stoller, L. Lai, S. Murali, S. Mcdonnell, B. Cleveger, R. M. Wallace, et al., "Nitrogen doping of graphene and its effect on quantum capacitance, and a new insight on the enhanced capacitance of N-doped carbon," *Energy Environ. Sci.* **5**, 9618 (2012).

[17] J. Zhu, A. S. Childress, M. Karakaya, S. Dandeliya, A. Srivastava, Y. Lin, A. M. Rao, and R. Podila, "Defect-Engineered Graphene for High-Energy- and High-Power-Density Supercapacitor Devices," *Adv. Mater.* (2016).

[18] A. Jorio, M. M. Lucchese, F. Stavale, E. H. M. Ferreira, M. V. O. Moutinho, R. B. Capaz, and C. A. Achete, "Raman study of ion-induced defects in N-layer graphene.," *J. Phys. Condens. Matter* **22**, 334204 (IOP Publishing, 2010).

[19] R. Podila, J. Chacón-Torres, J. T. Spear, T. Pichler, P. Ayala, and A. M. Rao, "Spectroscopic investigation of nitrogen doped graphene," *Appl. Phys. Lett.* **101**, 123108 (AIP Publishing, 2012).

[20] P. Y. Huang, C. S. Ruiz-Vargas, A. M. van der Zande, W. S. Whitney, M. P.

Levendorf, J. W. Kevek, S. Garg, J. S. Alden, C. J. Hustedt, et al., "Grains and grain boundaries in single-layer graphene atomic patchwork quilts," *Nature* **469**, 389–392 (Nature Publishing Group, 2011).

[21] J. Hu, X. Ruan, and Y. P. Chen, "Thermal conductivity and thermal rectification in graphene nanoribbons: A molecular dynamics study," *Nano Lett.* **9**, 2730–2735 (2009).

[22] I. Calizo, A. A. Balandin, W. Bao, F. Miao, and C. N. Lau, "Temperature dependence of the raman spectra of graphene and graphene multilayers," *Nano Lett.* **7**, 2645–2649 (2007).

[23] L. Baraton, Z. He, C. S. Lee, J. L. Maurice, C. S. Cojocaru, Y. H. Lee, and D. Pribat, "Study of Graphene Growth Mechanism on Nickel Thin Films" (Springer Berlin Heidelberg, 2012).

[24] L. Baraton, Z. B. He, C. S. Lee, C. S. Cojocaru, M. Châtelet, J.-L. Maurice, Y. H. Lee, D. Pribat, B. S. et al, et al., "On the mechanisms of precipitation of graphene on nickel thin films," *EPL (Europhysics Lett.* **96**, 46003 (IOP Publishing, 2011).

[25] S. Radic, N. K. Geitner, R. Podila, A. Käkinen, P. Chen, P. C. Ke, and F. Ding, "Competitive Binding of Natural Amphiphiles with Graphene Derivatives," *Sci. Rep.* **3**, 2273 (Macmillan Publishers Limited. All rights reserved, 2013).

[26] P.G. Klemens, *Carbon* **1994,** 32735